UC Berkeley

UC Berkeley Previously Published Works

Title

How Indium Nitride Senses Water

Permalink

https://escholarship.org/uc/item/49h7p40r

Authors

Jovic, Vedran

Moser, Simon

Ulstrup, Søren

et al.

How Indium Nitride Senses Water

Vedran Jovic,*[1,2] Simon Moser,*[2] Søren Ulstrup,[2] Dana Goodacre,[1] Emmanouil Dimakis,[3] Roland Koch,[2] Georgios Katsoukis,[4] Luca Moreschini,[2] Sung-Kwan Mo,[2] Chris Jozwiak,[2] Aaron Bostwick,[2] Eli Rotenberg,[2] Theodore D. Moustakas,[5] Kevin E. Smith[1,5]

[1] School of Chemical Sciences and Centre for Green Chemical Sciences, The University of Auckland, Auckland 1142, New Zealand.

[2] Advanced Light Source, Lawrence Berkeley National Laboratory, Berkeley, CA 94720, USA.

[3] Department of Electrical and Computer Engineering, Center of Photonics Research, Boston University, Boston, MA 02215, USA.

[4] Molecular Biophysics and Integrated Bioimaging, Lawrence Berkeley National Laboratory, Berkeley, CA 94720, USA.

[5] Department of Physics, Boston University, Boston, MA 02215, USA.

* Contributed equally

Keywords: Sensor, 2-dimensional electron gas (2DEG), ARPES, surface electronic potential, quantum well.

The unique electronic band structure of indium nitride InN, part of the industrially significant III-N class of semiconductors, offers charge transport properties with great application potential due to its robust *n*-type conductivity. Here we explore the water sensing mechanism of InN thin films. Using angle-resolved photoemission spectroscopy, core level spectroscopy and theory we derive the charge carrier density and electrical potential of a two-dimensional electron gas, 2DEG, at the InN surface and monitor its electronic properties upon *in-situ* modulation of adsorbed water. An electric dipole layer formed by water molecules raises the surface potential and accumulates charge in the 2DEG, enhancing surface conductivity. Our intuitive model provides a novel *route* toward understanding the water sensing mechanism in InN – and more generally for understanding sensing material systems beyond InN.

The III-N semiconductor family is the heart of an expanding multi-billion-dollar electronics industry – an industry driven by InGaN alloy systems in light emitting diode (LED) applications.[1]

1

Indium Nitride (InN) is an intensely studied member of this family, offering a high charge carrier mobility and small effective electron mass, and thus tremendous potential for photonics and high speed transistors operating at up to several THz.[1-4] Innovations in molecular beam epitaxy[5,6] and metal-organic chemical vapor deposition[7,8] have made large scale production of very high quality InN feasible, and necessitated a revision of the fundamental optical gap from 1.9 eV to ~0.69 eV.[9] In the wake of these developments, alloys of InN with other III-Ns allow for precise control of the band gap over a wide energy range, paving the way for applications such as high-brightness white LEDs, high frequency electronics and solar cells accepting infrared to UV light[10,11] In the infrared, InN based diodes even offer an environmentally benign alternative to GaAs based diodes.

An intriguing application for InN, in line with incentives to apply the system's robust *n*-type nature, is as a transducer in chemical- and bio-sensing.[12-15] The charge-neutrality level (CNL) in InN, is well above the conduction band minimum, resulting in intrinsic *n*-type charge carrier doping of the "as grown" material. This leads to surface band bending and the formation of a particularly prominent electron accumulation layer.[16] A quantum well (QW) forms, hosting a two-dimensional electron gas (2DEG) with quantized energy levels.[17] This QW is highly sensitive to surface adsorbates, which modulate the 2DEG and surface charge carrier concentration, resulting in a macroscopic resistance change in the semiconductor.[12] In addition to its robust yet electrically responsive surface properties, the biocompatible nature and thermal stability of InN make it an archetypal candidate for sensing applications – a rarely studied field for this material.[18]

Here we explore the sensing properties of InN explicitly with respect to water on an entirely quantum mechanical level; We achieve this by uniting soft X-ray angle-resolved photoemission spectroscopy (ARPES) and core level spectroscopy (XPS) to monitor the 2DEG of InN alongside its surface chemical composition. Figure 1 presents our central result. Specifically, Fig. 1 (a)

shows O 1s core level spectra on an N-polar InN film collected as a function of exposure time to 650 eV X-rays (where one scan is ~30 s). To mimic realistic device conditions, the film was pre-exposed to ambient humidity in air, followed by a mild annealing step in UHV to ensure sufficient surface quality for ARPES (as described in the experimental section). This produced an oxidized, slightly carbon contaminated surface (shown by the survey scan in Suppl. Fig. 1). In Fig. 1 (a), peak 'i.' at ~530.3 eV is characteristic of surface oxidation, i.e. of In-O.[19,20] The high-energy shoulder, peak 'ii', corresponds to OH groups – indicating significant amounts of dissociated H_2O. Peak 'iii.' at 533.6 eV on the other hand represents molecular water at the InN surface due to previous exposure to humidity.[21,22] A decrease in the spectral weight of peak 'iii' results from continuous desorption of water by the X-ray beam. This resulted in a shift of the main O 1s core level (peak 'i'), as well as the main peaks in the In 4d (Fig. 1 (b)), N 1s (c) and C 1s core levels (d) – collected simultaneously to the O 1s spectra – towards lower binding energies (as also shown by the insets of Figs. 1 (b-d). The shifts reflect a reduction in the degree of surface band bending. As the core level line-shapes remained unaffected by the X-rays (shown by the peak fitted spectra in Suppl. Fig. 2), we distinguish molecular water desorption from other effects, such as water association from H and OH, or the creation of defect states,[23] as the microscopic source of this energy shift (see the text related to Suppl. Fig. 1-2 for a deeper discussion of the related chemical phenomena).

Due to a remarkably high photoemission cross-section of the 2DEG at 650 eV incident X-ray energy (as discussed in detail for Fig. 2), we could measure ARPES of the valence band (VB) and 2DEG regions simultaneously to the core levels in plots (a-d). The VB and 2DEG spectra collected as a function of exposure time to the X-ray beam and integrated only over a small momentum range covering the 2DEG are shown in Fig. 1 (e). By comparison of the integrated spectral weight

of the 2DEG with the integrated spectra weights of the H_2O, surface oxygen and OH peaks in Fig.

1 (f), we find a direct link between the removal of adsorbed H_2O by X-ray exposure and

depopulation of the charge carrier density in the 2DEG. As we find out in more detail later, this is

due to an electric dipole field produced by H_2O molecules, enhancing the surface band bending.
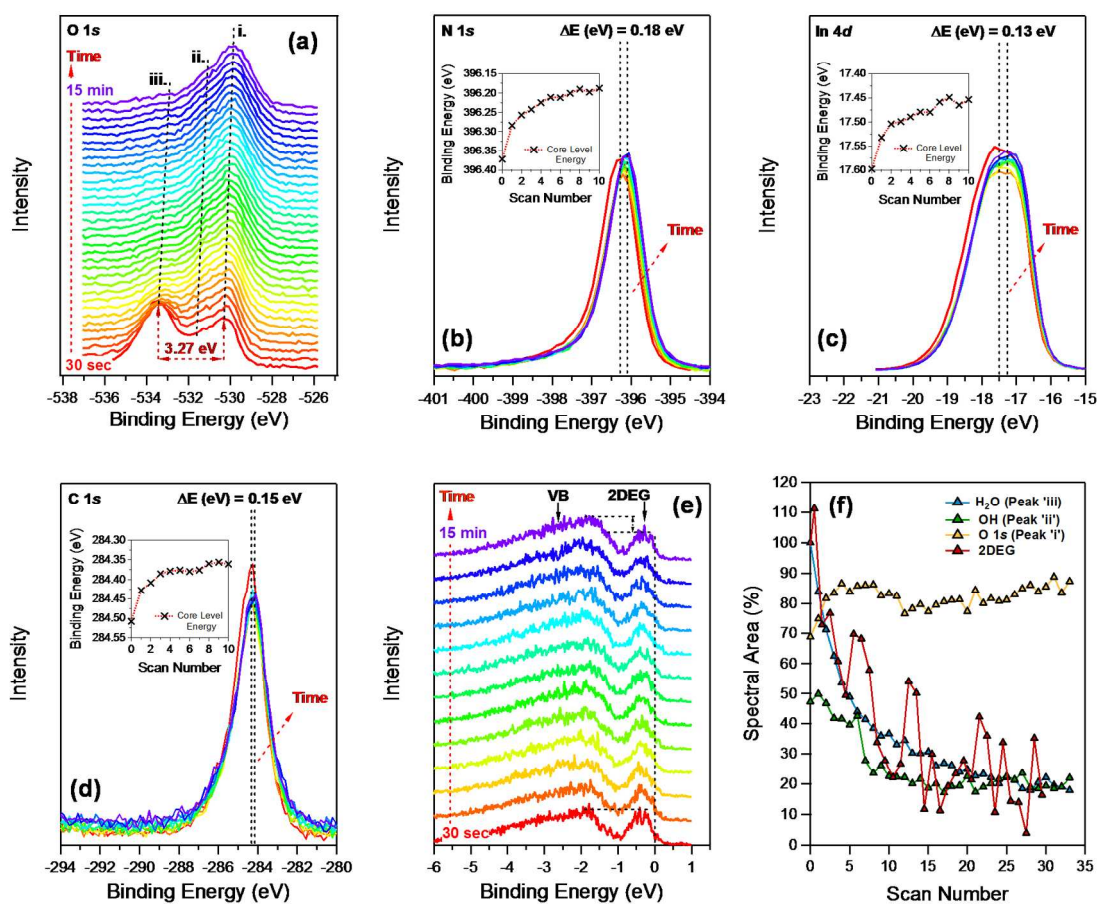
Figure 1. H_2O desorption from the surface of InN – (a) O $1s$ core level spectra as a function of exposure time to 650 eV X-rays. Peak 'i' is attributed to surface oxidation and peak 'iii' is attributed to adsorbed water. **(b)** Time dependent N $1s$ core level spectra upon X-ray irradiation. The inset summarizes the low energy shift in the peak position as a function of time. The equivalent spectra for the In $4d$ **(c)** and C $1s$ **(d)** core level regions. **(e)** The VB and CB (2DEG) region as a function of exposure time to 650 eV X-rays. **(f)** A comparison of the intensity of peak 'iii' associated to H_2O in (a) and the intensity of the 2DEG as a function of exposure time (one scan is ~30 s).

Having revealed that surface water directly controls the surface electron accumulation layer in InN, we will now examine the microscopic origin of this effect. We start by showing how high-resolution ARPES along with a simple and intuitive model can be used to access the fundamental performance gauges for gas sensing semiconductors,[14] i.e. the surface charge carrier density, and the shape of the surface potential. We will then use this knowledge to further probe the mechanism by which surface adsorbed water modulates these parameters.
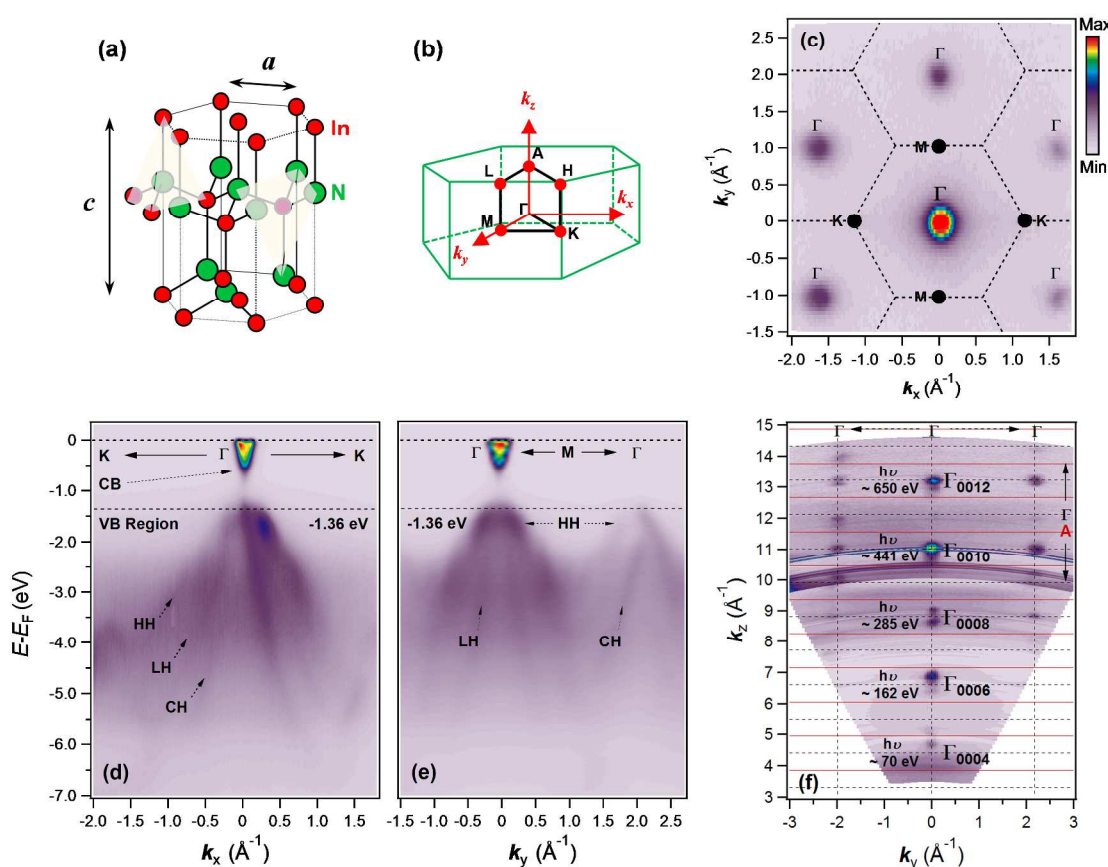

Figure 2. ARPES overview of the InN valence electrons – (a) Unit cell of wurtzite-type InN (a = 3.538 Å and c = 5.704 Å). **(b)** 3D bulk BZ of the unit cell. **(c)** ARPES Fermi surface over several surface BZs (black dashed lines) using 162 eV p-polarized photons. The high symmetry points are labelled. ARPES intensity maps along the ΓK **(d)** and ΓM **(e)** high symmetry directions show the VB region (E < -1.36 eV) and the CB (2DEG) ($h\nu$ = 162 eV, p-polarization). **(f)** A Fermi surface scan across an energy range of 32-800 eV, plotted using an inner potential of 18 eV. $h\nu$ represents incident X-ray photon energies where we see photoemission intensity from the 2DEG.

Figure 2 presents the InN structure along with an ARPES overview of its valence electrons. The wurtzite-type crystal structure of InN is shown in Fig. 2 (a), along with the bulk Brillouin zone (BZ) in Fig. 2 (b).[24] Along the *c*-axis, mirror symmetry is broken, thus, resulting in an intrinsically polar system. In Fig. 2 (c) we show a Fermi surface map measured over several surface BZs (black lines), with 162 eV *p*-polarized photons. At this photon energy, the Γ_{000}-point of the hexagonal surface BZ coincides with the Γ_{0006}-point of the bulk BZ. We observe circular electron pockets at the Γ-points, corresponding to a previously observed 2DEG in InN.[17,25] Cuts along the ΓK (k_x) and ΓM (k_y) high symmetry directions in Fig. 2 (c) are shown as E (eV) vs. $\boldsymbol{k}$ (Å^{-1}) ARPES intensity maps in Figs. 2 (d) and (e), respectively. The valence states ($E < -1.36$ eV) are composed of three hole-like bands of N $2p$ and In $5p$ character[16]: a heavy-hole (HH), a light-hole (LH) and a split-off hole band (CH), with the valence band (VB) maximum at -1.36 eV.[16,26] Close to the Fermi level (0 eV), we see a rapidly dispersing electron-like parabolic (conduction) band (CB) which forms the circular pockets of the 2DEG at the Γ-points in Fig. 2 (c). Its minimum is located at approximately -0.47 eV (see Suppl. Fig. 3. for a summary of the valence state energetic offsets), resulting in a direct band gap, E_g, of 0.89 eV, in line with calculations,[27,28] but larger than the two-particle optical gap of ~0.70 eV.[9,29]

The Fermi surface as a function of the out-of-plane momentum $\boldsymbol{k}_z$, measured over an X-ray energy range of 32-800 eV, is shown in Fig. 2 (f). Starting from Γ_{0004}, the 2DEG intensity recurs at even Γ-points (black horizontal lines) of the bulk BZs (red lines mark BZ boundaries), reflecting the out-of-plane periodicity π/c of the recurring InN layers. The $\boldsymbol{k}_z$ dispersion reveals a remarkable pseudo 3D character of the 2DEG. We will show below that this is indeed a direct consequence of the 2DEG wave functions penetrating significantly into the bulk. We also note the extraordinarily high photoemission cross-section of the 2DEG for photon energies all the way up to 800 eV (X-ray

6

energies corresponding to high photoemission cross-sections are labelled in (f)). This unusually

high cross-section allowed us to monitor variations in the 2DEG with water desorption while

simultaneously measuring core level XPS (requiring high incident X-ray energies) in Fig. 1. Thus,

this physical property offered us key insight into physiochemical processes related to the InN

water sensing mechanism.
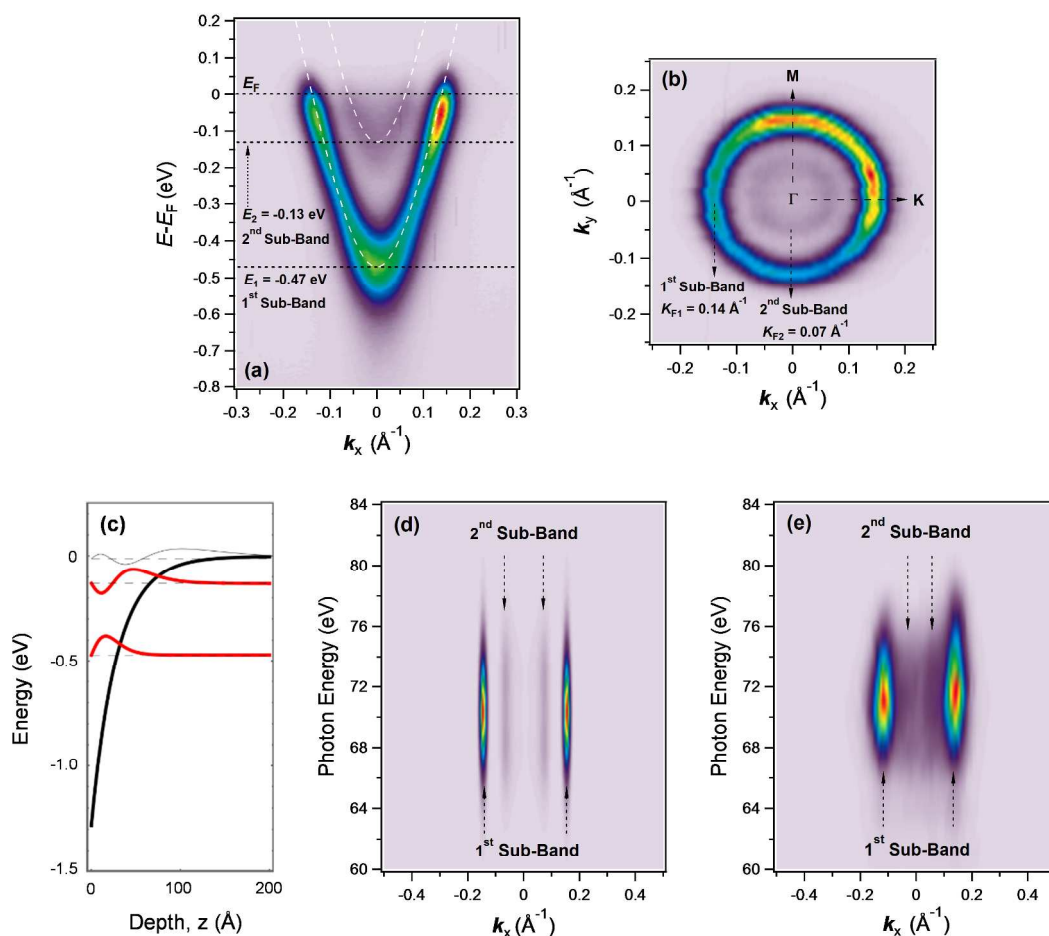
Figure 3. High resolution ARPES intensity maps of the 2DEG state and the calculated surface potential – (a) ARPES intensity map of the QW region showing the outer ('1st') and inner ('2nd') sub-bands, measured at hν = 70.5 eV in the *p*-polarization. **(b)** The corresponding ARPES Fermi surface map of the QW in (a). **(c)** Surface potential (black line) and wave functions (red lines) extracted using the QW model and experimental energy parameters obtained from (a). A third QW sub-band, ~10 meV below E_F, is shown in grey. A comparison of the calculated **(d)** and measured **(e)** photon energy dependent Fermi surface close to Γ_{0004}.

Figure 3 presents an in-depth analysis of the 2DEG. The ARPES map in Fig. 3 (a) identifies two pronounced sub-bands in the QW: the first with an energy minimum at $E_1 = -0.47$ eV, crossing the Fermi level at $\mathbf{k}_{F1} = 0.14$ Å^{-1}, and a second, weaker sub-band at $E_2 = -0.13$ eV with $\mathbf{k}_{F2} = 0.07$ Å^{-1}. Fitting the band dispersion within a standard Kane $\mathbf{k} \cdot \mathbf{p}$ approach[30] (white dashed lines in (a)), the effective electron masses for the first and second sub-band are found to be $m_1^* = 0.13 m_e$ and $m_2^* = 0.10 m_e$, respectively. A k_x-k_y Fermi surface map of Fig. 3 (a) is shown in (b), revealing circular contours from both the first and second sub-bands. From their area, we calculate a sheet carrier density of $n_e \sim 1.1 \times 10^{13}$ cm^{-2}. Extrapolating this result, we estimate a near-surface bulk density of $\sim 3.2 \times 10^{19}$ cm^{-3}. This value is consistent with our electronic transport data (5×10^{19} cm^{-3}), and suggests that bulk transport in InN is mostly mediated by the surface.

From the energies E_1 and E_2 of the two sub-bands, we gain further information on the precise shape of the QW potential hosting the 2DEG. Assuming an exponential surface potential well[31] $V(z) = -V_1 e^{-2z/a}$ with a depth of V_1 and a width of a, the energy E_i of subband i is given by the ith root of the Bessel function $J_{\alpha i}(\beta) = 0$, where $\alpha_i^2 = -(2 m_e a^2 E_i)/\hbar^2$, $\beta^2 = -(2 m_z a^2 V_1)/\hbar^2$, and $m_z \sim 0.09 m_e$ is the out-of-plane effective electron mass.[32] Solving numerically for E_1 and E_2, we find a surface potential depth of $V_1 \sim 1.3$ eV and a width a of ~ 58 Å (~ 10 unit cells (u.c.)). From the associated QW potential, $V(z)$ (black solid line in Fig. 3 (c)), all additional bound state energies E_i as well as their corresponding wave function solutions $\Psi(z) = J_{\alpha i}(\beta e^{-z/a})$ can be determined (red solid lines in Fig. 3 (c)). Calculating their quantum-mechanical expectation values, we find the charge density of sub-band Ψ_1 to be localized around ~ 20 Å, i.e. 3.5 u.c. below the surface, while the second sub-band Ψ_2 is located on average ~ 48 Å, i.e. 8.5 u.c. below the surface. Notably, our simulations also predict a third sub-band at $E_3 \sim -10$ meV, located ~ 115 Å, ~ 20 u.c., below the surface (grey line in Fig. 3 (c)). Due to its bulk-like nature, it only shows diffuse spectral weight

8

close to the Fermi level in Figs. 3 ((a), (d) and (e)). This is reasonable if we consider that up to four

sub-bands have been experimentally shown by our group on InN films with higher charge carrier

concentrations.[33] From the Fourier transform of Ψ, we further predict the k_z dependence of the

Fermi surface, shown in Fig. 3 (d), and compare it to the experimental ARPES result around Γ_{0004}

in Fig. 3 (e). Details of our model are presented in the Suppl. Material.

The excellent agreement in between experiment and theory confirms that this model reliably

accesses key parameters of the surface QW, and can thus be used as a reliable probe of changes in

the 2DEG induced by surface-water interactions. We thus repeat the beam-dosing experiment

from Fig. 1. However, this time we use ARPES with an X-ray energy of 70.5 eV (as in Fig. 3), and

thus we strongly enhance the energy and the momentum resolution. This allows us to probe

detailed changes in the surface potential with water desorption. In contrast to the data in Fig. 3,

however, the following data is collected using a higher X-ray flux density – to achieve water

desorption in a controlled but continuous way.
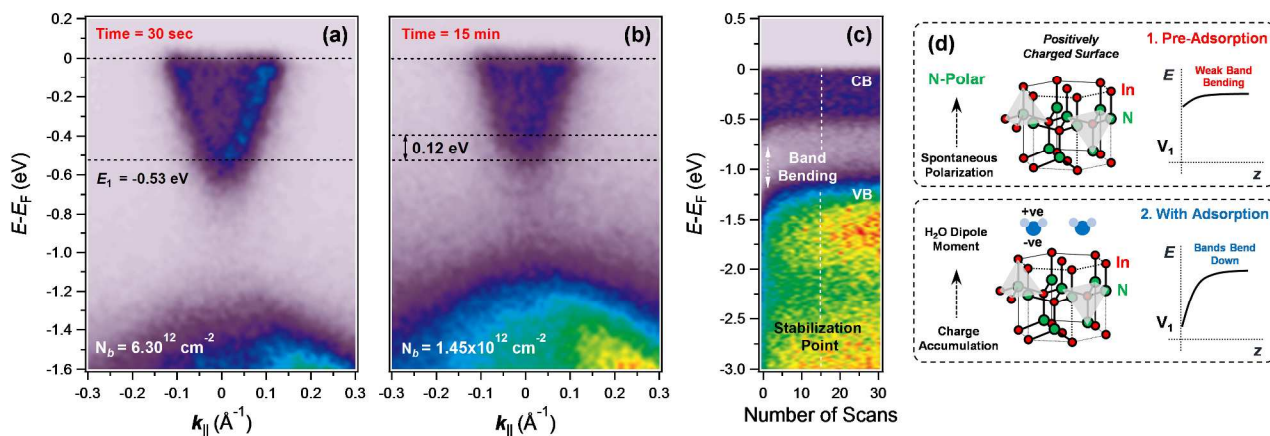
Figure 4 The mechanism of water sensing by InN – ARPES intensity map of the 2DEG before **(a)** and after **(b)** desorption of water by exposure to 70.5 eV X-rays. **(c)** Corresponding decrease in downward band bending with water desorption. **(d)** Proposed mechanism for the alignment of electric dipoles with the N-polar surface of InN resulting in electron accumulation and downward band bending upon water adsorption.

Figure 4 (a) shows an ARPES map of the 2DEG state in an N-polar InN film at the onset of X-ray irradiation. Figure 4 (b) shows the same 2DEG state after 15 min of X-ray beam exposure. Comparing the spectra, we observe a rigid 120 meV upward shift of the 2DEG state. Furthermore, we observe a depletion of the 2DEG from $n_e \sim 6.3 \times 10^{12}$ cm^{-2} (at the onset of X-ray exposure) to 1.5×10^{12} cm^{-2} (after 15 min of exposure). Since this shift is rigid, and bulk screening effects are unlikely to be affected by adsorbents, the QW width a can be safely assumed to remain unaffected, while water desorption reduces the surface potential from $V_1 = 1.4$ eV to $V_1 = 1.2$ eV in this sample (see the discussion relating to Suppl. Fig. 4 for details on the extraction of these values).

What is the microscopic origin of this potential modulation? – In principle, water might act as an electron donor to the QW, populating the 2DEG.[34] However, this would vary the oxidation state of In and N at the surface. The associated core levels along with the O 1s core level (all shown in Fig. 1 along with the peak fitted data in Suppl. Fig. 2) remained unaffected by the X-ray beam. Charge transfer processes from the adsorbent to the substrate are consequently ruled out, in contrast to earlier studies of oxygen, potassium and water interactions with InN.[19,35] We suggest a more *universal* scenario based on a model involving the spontaneous polarization of the InN film, and the electric dipole of water molecules.[36]

In InN of N-polarity, bonds starting from the substrate are ordered from N to In. Thus, the orientation of spontaneous polarization points from the substrate to the surface of the film, making the free surface positively charged (this scenario is shown in Fig. 4 (d), top panel). Consequently, polar H_2O molecules will stick to the free surface through the negatively charged O atoms. In this case, the H_2O electric dipole moment (1.9 Debye) will direct away from the surface of the film (as depicted in the bottom panel of Fig. 4 (d)). The electric field of the system now points inwards and

10

draws additional charge from the bulk into the electron accumulation layer, populating the 2DEG. This results in further downward band bending. A similar electric field effect is routinely exploited to regulate charge accumulation layers in ionic liquid doped systems.[13,14] We argue that a similar, albeit much weaker effect, is also obtained from H_2O adsorption, likely due to a directed alignment of the water dipoles on the surface (see Suppl. Fig. 5).

In summary, we employed ARPES in unison with core level spectroscopy to investigate the water sensing mechanism in InN. We demonstrate that a well-pronounced and robust 2DEG at the surface of InN serves as a water sensing monitor. A simple and intuitive QW model provides direct access to the surface charge carrier density as well as the surface potential upon water adsorption. We suggest that water at the surface of InN fosters an electric field effect, promoting downward band bending and electron accumulation with up to a six-times increased carrier concentration in the 2DEG. Our unique approach provides novel routes towards an advanced understanding of surface ad-layers on a series of materials important for sensing applications.

Experimental Section

InN films were grown on (0001) (*c*-plane) sapphire substrates by radio frequency plasma-assisted molecular beam epitaxy (PAMPE).[36,37] The 0.5-1 μm thick films were nominally N-polar and intrinsically *n*-type ($\sim 5 \times 10^{19}$ cm^{-3}), with electron mobility's of approximately 400 cm^2/V.s and an experimentally determined room temperature optical gap of 0.77 eV.[37]

ARPES measurements were performed at ARPES beamline 10.0.1 and at the Microscopic And Electronics STRucture Observatory (MAESTRO) at beamline 7.0.2 of the Advanced Light Source, Lawrence Berkeley National Laboratory. The energy and momentum resolution were set to < 10 meV and 0.01 Å^{-1}. Films were annealed in ultra-high vacuum ($\sim 1 \times 10^{-11}$ torr) at 300 ^{o}C for

~30 min prior to measurements. All data was collected at temperatures between 10-90 K. Binding energies were referenced to the measured Fermi level of a tantalum or a copper block in direct electrical contact with the sample.

The photon energy dependent ARPES Fermi surface was collected over a photon energy range of 32-800 eV at normal emission, $k_\parallel = 0$ Å^{-1}. The intensity has been normalized to the total electron current and is plotted as a function of the out-of-plane momentum k_z (Å^{-1}) (probing along the Γ-A direction), using an inner potential V_0 of 18 eV.

Acknowledgments

Supporting Information.

An in-depth discussion on the nature of the InN surface-water interaction from an angle-integrated XPS perspective; Discussion on the possible role of defect chemistry on the charge carrier density in the 2DEG; Summary of the energetic offsets related to the valence states near the Fermi level; Theoretical model describing photoemission spectra from the 2DEG; Extracted surface potential diagrams before and after water desorption from the surface; Further proposed mechanism for the alignment of electric dipoles of water with the InN surface.
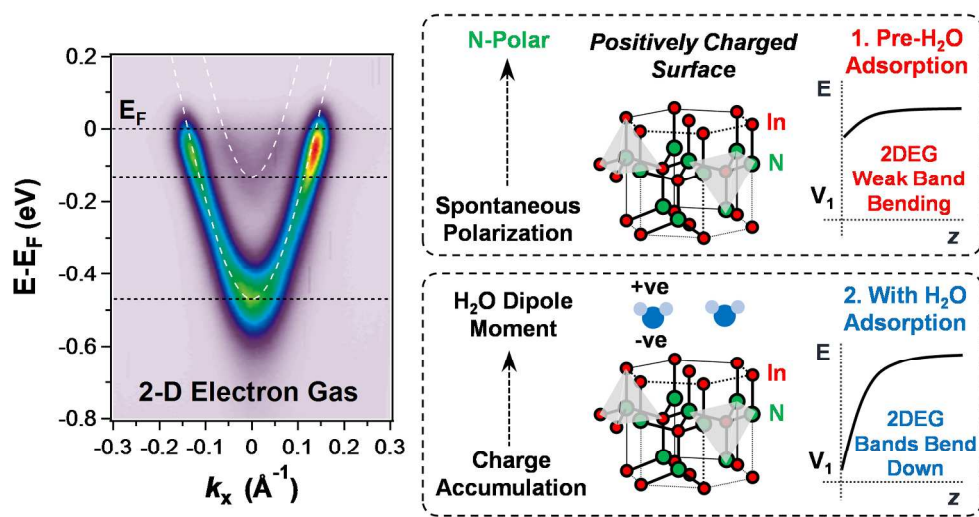
References

1.   Wu, J. *J. Appl. Phys.* **2009**, *106*, 011101.

2.   Bhuiyan, A. G.; Hashimoto, A.; Yamamoto, A. *J. Appl. Phys.* **2003**, *94*, 2779.

3.   *Indium Nitride and Related Alloys*; Veal, T. D., McConville, C. F., Schaff, W. J., Eds.; CRC Press Taylor & Francis Group: Boca Raton, London, New York, 2010.

4.   O'Leary, S.; Foutz, B. E.; Shur, M. S.; Eastman, L. F. *Appl. Phys. Lett.* **2006**, *88*, 152113.

5.   Lu, H.; Schaff, W. J.; Hwang, J.; Wu, H.; Koley, G.; Eastman, L. F. *Appl. Phys. Lett.* **2001**, *79*, 1489.

6.   Nanishi, Y.; Saito, Y.; Yamaguchi, T. *Jpn. J. Appl. Phys.* **2003**, *42*, 2549–2559.

7.   Huang, Y.; Wang, H.; Sun, Q.; Chen, J.; Li, D. Y.; Wang, Y. T.; Yang, H. *J. Cryst. Growth* **2005**, *276*, 13–18.

8.   Yamamoto, A.; Tanaka, T.; Koide, K.; Hashimoto, A. *Phys. Status Solidi* **2002**, *194*, 510–514.

9.   Davydov, V. Yu.; Klochikhin, A. A.; Seisyan, R. P.; Emtsev, V. V.; Ivanov, S. V.; Bechstedt, F.; Furthmuller, J.; Harima, H.; Mudryi, A. V.; Aderhold, J.; Semchinova, O.; Graul, J. *Phys. Stat. Sol.* **2002**, *229*, R1-R3.

10.   Pan, W.; Dimakis, E.; Wang, G. T.; Moustakas, T. D.; Tsui, D. C. *Appl. Phys. Lett.* **2014**, *105*, 213503.

11.   Dimakis, E.; Thomidis, C.; Zhou, L.; Smith, D. J.; Abell, J.; Moustakas, T. D. *Phys. Status Solidi A* **2008**, *205*, 1070–1073.

12.   Lu, H.; Schaff, W. J.; Eastman, L. F. *J. Appl. Phys*. **2004**, *96*, 3577.

13.   Lu, Y.; Ho, C.; Yeh, J. A.; Lin, H.; Gwo, S. *Appl. Phys. Lett.* **2008**, *92*, 212102.

14.   Chaniotakis, N.; Sofikiti, N. *Anal. Chim. Acta* **2008**, *615*, 1–9.

15.   Eisenhardt, A.; Krischok, S.; Himmerlich, M. *Phys. Rev. B* **2015**, *91*, 245305.

16.   King, P. D. C.; Veal, T. D.; Jefferson, P. H.; Hatfield, S. A.; Piper, L. F. J.; McConville, C. F.; Fuchs, F.; Furthmuller, J.; Bechstedt, F.; Lu, H.; Schaff, W. J. *Phys. Rev. B* **2008**, *77*, 045316.

17.   Colakerol, L.; Veal, T. D.; Jeong, H.; Plucinski, L.; Demasi, A.; Learmonth, T.; Glans, P.; Wang, S.; Zhang, Y.; Piper, L. F. J.; Jefferson, P. H.; Fedorov, A.; Chen, T.; Moustakas, T. D.; McConville, C. F.; Smith, K. E. *Phys. Rev. Lett.* **2007**, *97*, 237601.

18.   Chang, Y.-H.; Lu, Y-S.; Yeh, J. A.; Hong, Y-L.; Lee, H-M.; Gwo, S. InN-Based Chemical Sensors. In *Semiconductor Device-Based Sensors for Gas, Chemical and Biomedical Applications*; Ren, F., Pearton, S. J., Eds.; CRC Press Taylor & Francis Group, Boca Raton, London, New York, 2011; pp 131–146.

19. Eisenhardt, A.; Reiß, S.; Himmerlich, M.; Schaefer, J. A.; Krischok, S. *Phys. Status Solidi A* **2010**, *207*, 1037–1040.

20. Butcher, K. S. A.; Fernandes, A. J.; Chen, P. P.-T.; Wintrebert-Fouquet, M.; Timmers, H.; Shrestha, S. K.; Hirshy, H.; Perks, R. M.; Usher, B. F. J. Appl. Phys. 2007, 101 (123702), 1–11.

21. Zhang, X.; Ptasinska, S. *J. Phys. Chem. C* **2014**, *118*, 4259–4266.

22. Yamamoto, S.; Kendelewicz, T.; Newberg, J. T.; Ketteler, G.; Starr, D. E.; Mysak, E. R.; Andersson, K. J.; Ogasawara, H.; Bluhm, H.; Salmeron, M.; Brown, G. E.; Nilsson, A. *J. Phys. Chem. C* **2010**, *114*, 2256–2266.

23. Van de Walle C. G.; Lyons, J. L.; Janotti, A. *Phys. Status Solidi A* **2010**, *207*, 1024–1036.

24. Paszkowicz, W.; Cerny, R.; Krukowski, S. *Powder Diffr.* **2016**, *18*, 114–121.

25. Meevasana, W.; King, P. D. C.; He, R. H.; Mo, S.; Hashimoto, M.; Tamai, A.; Songsiriritthigul, P.; Baumberger, F.; Shen, Z. *Nat. Mater.* **2011**, *10*, 114–118.

26. Yeo, Y. C.; Chong, T. C.; Li, M. F. *J. Appl. Phys.* **1988**, *83*, 1429.

27. Wei, S.-H., Nie, X., Batyrev, I. G. & Zhang, S. B. *Phys. Rev. B* **2003**, *67*, 165209.

28. Bagayoko, D.; Franklin, L. *J. Appl. Phys.* **2005**, *97*, 123708.

29. Wu, J.; Walukiewicz, W.; Shan, W.; Yu, K. M.; Ager, J. W. *J. Appl. Phys.* **2003**, *94*, 4457.

30. Kane, E. O. *J. Phys. Chem. Solids* **1957**, *1*, 249–261.

31. Buckingham, R. A. Exactly Soluble Bound State Problems. In *Quantum Theory*; Bates, D. R.; Academic Press: New York, 1961; pp 81–121.

32. Hofmann, T.; Chavdarov, T.; Darakchieva, V.; Lu, H.; Schaff, W. J.; Schubert, M. *Phys. Status Solidi* **2006**, *3*, 1854–1857.

33. Colakerol, L.; Piper, L.F.J.; Fedorov, A.; Chene, T.; Moustakas, T. D.; Smith, K. E. *Surf. Sci.* **2015**, *632*, 154–157.

34. Janotti, A.; Van de Walle, C. G. *Nat. Mater.* **2007**, *6*, 44–47.

35. Reiß, S.; Eisenhardt, A.; Krischok, S.; Himmerlich, M. *Phys. Status Solidi* **2014**, *11*, 428–431.

36. Stutzmann, M.; Steinhoff, G.; Eickhoff, M.; Ambacher, O.; Nebel, C. E.; Schalwig, J.; Neuberger, R.; Müller, G. *Diam. Relat. Mater.* **2002**, *11*, 886–891.

37. Chen, T. P.; Thomidis, C.; Abell, J.; Li, W.; Moustakas, T. D. *J. Cryst. Growth* **2006**, *288*, 254–260.

38. Wang, Y.; Özcan, A. S.; Özaydin, G.; Ludwig, K. F. Jr.; Bhattacharyya, A.; Moustakas, T. D.; Zhou, H.; Randall L. H.; Siddons, D. P. *Phys. Rev. B* **2006**, *74*, 235304.

1
2
3
4
5
6
7
8
9
10
11
12
13
14
15
16
17
18
19
20
21
22
23
24
25
26
27
28
29
30
31
32
33
34
35
36
37
38
39
40
41
42
43
44
45
46
47
48
49
50
51
52
53
54
55
56
57
58
59
60

15

1
2
3
4
5
6
7
8
9
10
11
12
13
14
15
16
17
18
19
20
21
22
23
24
25
26
27
28
29
30
31
32
33
34
35
36
37
38
39
40
41
42
43
44
45
46
47
48
49
50
51
52
53
54
55
56
57
58
59
60

230x126mm (240 x 240 DPI)